Assessing the significance of fidelity as a figure of merit in quantum state reconstruction of discrete and continuous-variable systems

Antonio Mandarino,[1] Matteo Bina,[1,*] Carmen Porto,[1] Simone Cialdi,[1,2] Stefano Olivares,[1,2] and Matteo G. A. Paris[1,2]
[1]*Dipartimento di Fisica, Università degli Studi di Milano, I-20133 Milan, Italy*
[2]*Istituto Nazionale di Fisica Nucleare, Sezione di Milano, I-20133 Milan, Italy*
(Received 5 April 2016; published 20 June 2016)

We experimentally address the significance of fidelity as a figure of merit in quantum state reconstruction of discrete (DV) and continuous-variable (CV) quantum optical systems. In particular, we analyze the use of fidelity in quantum homodyne tomography of CV states and maximum-likelihood polarization tomography of DV ones, focusing attention on nonclassicality, entanglement, and quantum discord as a function of fidelity to a target state. Our findings show that high values of fidelity, despite well quantifying geometrical proximity in the Hilbert space, may be obtained for states displaying opposite physical properties, e.g., quantum or semiclassical features. In particular, we analyze in detail the quantum-to-classical transition for squeezed thermal states of a single-mode optical system and for Werner states of a two-photon polarization qubit system.

DOI: 10.1103/PhysRevA.93.062118

I. INTRODUCTION

In quantum technology, it is very common to summarize the results of a reconstruction technique, either full quantum tomography [1–7] or some partial reconstruction scheme [8–13], by the use of fidelity [14,15]. Once the information about the state of a system has been extracted from a set of experimental data, the fidelity between the reconstructed state and a given target state, is calculated [16–19]. Fidelity is bounded to the interval $[0,1]$. High values such as 0.9 or 0.99 are thus considered as a piece of evidence in order to certify that the reconstructed and the target states (i) are very close each other in the Hilbert space and (ii) they share nearly identical physical properties. In this framework, quantum resources of the prepared state are often benchmarked in terms of fidelity [20–25], e.g., to assess the performances of a teleportation scheme [26,27].

The two statements above may appear rather intuitive, with the second one following from the first one. On the other hand, it has been suggested that the use of fidelity may be misleading in several situations involving either discrete or continuous variable systems [28–31]. The main goal of the present paper is to experimentally confirm the first statement and, at the same time, to provide neat examples where the second one is clearly proved wrong.

Given two quantum states described by density matrices $\hat{\rho}_1$ and $\hat{\rho}_2$, the fidelity between them is defined as [14]

$$F(\hat{\rho}_1,\hat{\rho}_2) = \mathrm{Tr}\left[\sqrt{\sqrt{\hat{\rho}_1}\hat{\rho}_2\sqrt{\hat{\rho}_1}}\right]^2. \tag{1}$$

Fidelity is not a proper distance in the Hilbert space. However, it can be easily linked to a distance, and in turn to a metric over the manifold of density matrices. In fact, the Bures distance [32] between two states is defined as

$$D_B(\hat{\rho}_1,\hat{\rho}_2) = \sqrt{2[1-\sqrt{F(\hat{\rho}_1,\hat{\rho}_2)}]}.$$

Fidelity also provides an upper and a lower bound to the trace distance, namely [15]

$$1-\sqrt{F(\hat{\rho}_1,\hat{\rho}_2)} \leqslant \tfrac{1}{2}||\hat{\rho}_1-\hat{\rho}_2||_1 \leqslant \sqrt{1-F(\hat{\rho}_1,\hat{\rho}_2)}.$$

These relationships ensure that higher values of fidelity correspond to geometrical proximity of the two states in the Hilbert space. However, they do not seem straightforwardly related to the physical properties of the two states. In turn, it has been pointed out [28–31] that a pair of states that appear very close to each other in terms of fidelity may be very far in terms of physical resources. Relevant examples may be found with bipartite systems of either qubits or CV Gaussian states, where pairs of states composed of one entangled and one separable state may have (very) high value of fidelity one to each other. Besides, for single-mode CV states high values of fidelity may be achieved by pairs including one state with a classical analog and a genuinely quantum state of the field.

In this paper, we address the problem experimentally and analyze in detail the significance of fidelity as a figure of merit to assess the properties of a tomographically reconstructed state. We address both discrete and continuous variable systems using quantum homodyne tomography to reconstruct CV states and maximum-likelihood polarization tomography for DV ones. In particular, we experimentally address two relevant examples: (i) the reconstruction of squeezed thermal states of a single-mode radiation field, analyzing in details the quantum-to-classical transition, and (ii) the reconstruction of noisy Werner states of a two-qubit polarization system, inspecting the amount of nonclassical correlations. Our results clearly show that high values of fidelity, despite well quantifying geometrical closeness between states in the Hilbert space, may be obtained for quantum states displaying very different physical properties, e.g., quantum resources.

The paper is structured as follows. Section II is devoted to continuous variables: we first describe the experimental generation of single-mode squeezed thermal states using a seeded optical amplifier, as well as the homodyne technique employed for tomography. We then present experimental results, illustrating in detail the significance of the fidelity of the reconstructed state to a target one and its nonclassicality. In Sec. III we illustrate the experimental setup for generating two-qubit states of Werner type and the method of maximum-likelihood estimation for tomography. We then present experimental results, analyzing the significance of fidelity of the reconstructed states to the target Werner ones in

*Corresponding author: matteo.bina@gmail.com

assessing their nonclassical correlations, either entanglement or quantum discord. Section IV closes the paper with some concluding remarks.

II. SINGLE-MODE GAUSSIAN STATES

In this section we deal with the generation and the characterization of squeezed thermal states (STS) of a single-mode radiation field, i.e., states of the form

$$\hat{\rho} = \hat{S}(r)\hat{\nu}(n_{\rm th})\hat{S}^{\dagger}(r), \tag{2}$$

where $\hat{S}(r) = \exp\{\frac{1}{2}r[(\hat{a}^{\dagger})^2 - \hat{a}^2]\}$ is the squeezing operator, with $r \in \mathbb{R}$, $\hat{\nu}(n_{\rm th}) = n_{\rm th}^{\hat{a}^{\dagger}\hat{a}}/(1+n_{\rm th})^{\hat{a}^{\dagger}\hat{a}+1}$ is a thermal state with $n_{\rm th}$ average number of photons and $[\hat{a},\hat{a}^{\dagger}] = 1$, $\hat{a}$ and $\hat{a}^{\dagger}$ being field operators. Upon defining the quadrature operators

$$\hat{x}_{\theta} \equiv \hat{a}\, e^{-i\theta} + \hat{a}^{\dagger}\, e^{i\theta}, \tag{3}$$

with $\theta \in [0,\pi]$, the STS are fully characterized by their first and second moments

$$\langle \hat{x}_{\theta} \rangle = 0 \quad \forall\theta, \tag{4a}$$

$$\langle \Delta\hat{x}_{\theta}^2 \rangle = (1+2n_{\rm th})(e^{2r}\cos^2\theta + e^{-2r}\sin^2\theta), \tag{4b}$$

where $\langle \cdots \rangle \equiv {\rm Tr}[\hat{\rho}\cdots]$. In terms of the canonical operators $\hat{x} \equiv \hat{x}_0$ and $\hat{p} \equiv \hat{x}_{\pi/2}$, the covariance matrix (CM) of a STS reads

$$\sigma = \begin{pmatrix} \langle \Delta\hat{x}^2 \rangle & 0 \\ 0 & \langle \Delta\hat{p}^2 \rangle \end{pmatrix} = \begin{pmatrix} s/\mu & 0 \\ 0 & 1/\mu s \end{pmatrix}, \tag{5}$$

where $\mu = {\rm Tr}[\hat{\rho}^2] = (2n_{\rm th}+1)^{-1}$ is the purity of the state $\hat{\rho}$ and $s \equiv e^{2r}$ is the squeezing factor. A STS is nonclassical, i.e., it corresponds to a singular Glauber P function, whenever the conditions $s < \mu$ or $s > \mu^{-1}$ are satisfied. The total energy of a STS is given by

$$N_{\rm tot} = \langle \hat{a}^{\dagger}\hat{a} \rangle = n_{\rm th} + n_{\rm s} + 2n_{\rm th}n_{\rm s}, \tag{6}$$

where $n_s = \sinh^2 r$ is the number of squeezing photons and $n_{\rm th}$ is the thermal contribution to energy.

According to Eq. (6), it is possible to find a suitable parametrization of the single-mode STS CM (5) in terms of the different energy contributions

$$\langle \Delta\hat{x}^2 \rangle = \left(1 + 2\frac{N_{\rm tot} - n_{\rm s}}{2n_{\rm s}+1}\right)\left(1 + 2n_s - 2\sqrt{n_{\rm s}+n_{\rm s}^2}\right), \tag{7a}$$

$$\langle \Delta\hat{p}^2 \rangle = \left(1 + 2\frac{N_{\rm tot} - n_{\rm s}}{2n_{\rm s}+1}\right)\frac{1}{\left(1 + 2n_{\rm s} - 2\sqrt{n_{\rm s}+n_{\rm s}^2}\right)}, \tag{7b}$$

from which the linear behavior of the variances as a function of the total energy $N_{\rm tot}$ is apparent.

The fidelity between two STS is given by [33]

$$F(\sigma_1,\sigma_2) = \frac{1}{\sqrt{\Delta+\delta}-\sqrt{\delta}}, \tag{8}$$

where $\Delta = \frac{1}{4}\det[\sigma_1+\sigma_2]$ and $\delta = \frac{1}{4}\prod_{i=1,2}(\det\sigma_i - 1)$.

A. Experimental setup

In order to generate STS we employ the experimental setup schematically depicted in Fig. 1(a). It consists of three stages:

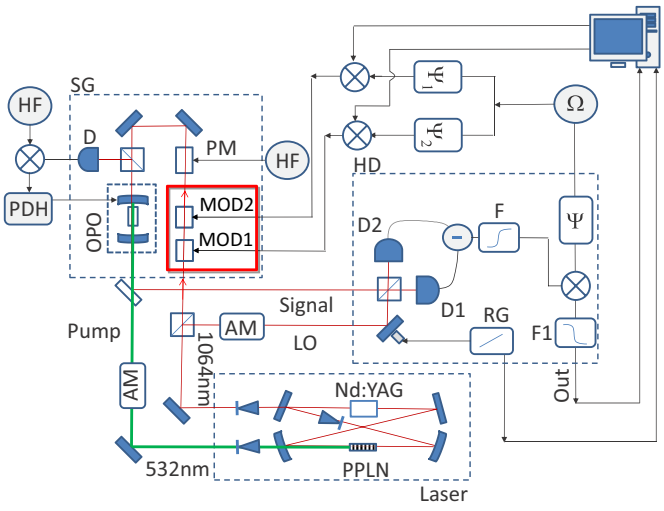

(a)

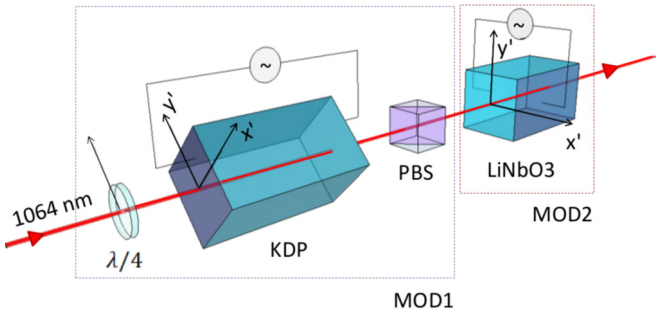

(b)

FIG. 1. (a) Schematic diagram of the experimental setup to generate squeezed thermal states. See text for details. (b) Generation stage of the OPO input signals. Two optical systems, MOD1 and MOD2, are collinear with the direction of propagation of the laser beam (1064 nm) and are positioned to sequentially intercept it. The laser beam at 1064 nm is sent to MOD1 which consists of a $\lambda/4$ plate, a KDP crystal, and a PBS: the optical field is prepared with circular polarization by setting the fast axis of $\lambda/4$ at an angle of 45° with respect to the incident p polarization, and then is passed through a KDP crystal whose axes are oriented at 45°. The horizontal component of the output beam selected by the PBS is sent in MOD2, which consists of a $LiNbO_3$ crystal whose extraordinary axis is horizontal.

laser, signal generator (SG), and homodyne detector (HD). Our source is a homemade internally frequency doubled Nd:YAG laser. It is based on a four mirrors ring cavity and the active medium is a cylindrical Nd:YAG crystal (diameter 2 mm and length 60 mm) radially pumped by three array of water-cooled laser diodes at 808 nm. The crystal for the frequency doubling is a periodically poled $MgO:LiNbO_3$ (PPLN) of 10 mm thermally stabilized (∼70 °C). Inside the cavity is placed a light diode that consists of a half-wave plate (HWP), a Faraday rotator (15°), and a Brewster plate (BP) in order to obtain the single mode operation.

The laser output at 532 nm is used as the pump for an optical parametric oscillator (OPO), while the output at 1064 nm is split into two beams by using a polarizing beam splitter (PBS): one is used as the local oscillator (LO) for the homodyne

detector and the other as the input for the OPO. The OPO cavity is linear with a free spectral range (FSR) of 3300 MHz, the output mirror has a reflectivity of 92%, and the rear mirror 99%. A phase modulator (PM) generates a signal at frequency of 110 MHz (HF) used as active stabilization of the OPO cavity via the Pound-Drever-Hall (PDH) technique [34,35]: the reflected beam from cavity is detected (D) and used to generate the error signal of PDH apparatus. This signal error drives a piezo connected to the rear mirror of the OPO cavity to actively control its length.

The homodyne detector (HD) consists of a 50:50 beam splitter, two low noise detectors, and a differential amplifier based on a LMH6624 operational amplifier. The visibility of the interferometer is about 98%. The quantum efficiency of the detector is about 95%, as specified in manufacturer data sheets of our detectors. To remove the low frequency signal we use a high-pass filter at 500 kHz and then the signal is sent to the demodulation apparatus. The information about the signal, at a frequency $\Omega \simeq 3$ MHz, is retrieved by using an electronic apparatus which consists of a mixer, a phase shifter Ψ set to ensure zero phase shift between the two inputs of the mixer, and a low-pass filter at 300 kHz. The electronic noise is 17 dB below the vacuum noise at 3 MHz for 10 mW of the LO power. The LO phase is spanned between 0 and 2π thanks to a piezomounted mirror linearly driven by a ramp generator (RG).

Our goal is to study a single-mode squeezed thermal state and therefore we have to generate a thermal seed to be injected into the OPO. The density matrix of thermal state in the Glauber representation reads as follows:

$$\hat{\nu}_{\mathrm{OPO}}(\tilde{n}_{\mathrm{th}}) = \int_0^\infty d|\alpha| \frac{2|\alpha|}{\tilde{n}_{\mathrm{th}}} e^{-\frac{|\alpha|^2}{\tilde{n}_{\mathrm{th}}}} \int_0^{2\pi} \frac{d\phi}{2\pi} ||\alpha|e^{i\phi}\rangle\langle|\alpha|e^{i\phi}|, \tag{9}$$

i.e., it can be viewed as a mixture of coherent states with phase ϕ uniformly distributed over the range 0 to 2π, and a given amplitude $|\alpha|$ distribution. Therefore, we have to generate a rapid sequence of coherent states with $|\alpha|$ and ϕ randomly selected from these distributions. It is worth noting that the parameter $\tilde{n}_{\mathrm{th}}$ does not coincide with the number of thermal photons n_{th} in Eq. (6), as the former is related to the thermal seeding of the OPO, whereas the latter accounts for both the seeding and any losses from the OPO to the detector.

Our strategy is to exploit the combined effect of the two optical systems [MOD1 and MOD2 in Fig. 1(a) described in Ref. [36] and sketched in more detail in Fig. 1(b)]. MOD1 generates a coherent state with phase 0, while MOD2 generates a coherent state with phase $\frac{\pi}{2}$. By matching these coherent states with properly chosen amplitudes, it is possible to generate an arbitrary coherent state. In order to control this process via pc, the MOD1 and MOD2 are driven by two identical electronic circuits which consist of a phase shifter $\Psi_{1,2}$ and a mixer. The pc processes the $|\alpha|$ and ϕ values of the coherent state which we want to generate, and converts them into voltage signals. These are sent to the mixer together with the sinusoidally varying signals at frequency Ω in order to obtain the right modulation signals on MOD1 and MOD2, while Ψ_1 and Ψ_2 are set so that these modulation signals are in phase when they reach MOD1 and MOD2.

Finally, in order to obtain the desired thermal state, the pc generates random $|\alpha|$ and ϕ values according to their specified distributions [see Eq. (9)] and converts them in two simultaneous trains of voltage values which are sent to the crystals in a time window of 70 ms with a repetition rate of 100 kHz. Generation and acquisition operations are synchronized in the same time window at the same sampling rate. Therefore, we collect 7000 homodyne data points $\{(\theta_k, x_k)\}$, LO phase, and quadrature value, respectively. The sampling is triggered by a signal generated by RG to ensure the synchronization between the acquisition process and the scanning of LO with $\theta_k \in [0, 2\pi]$.

Notice that seeding the OPO is a crucial step to observe the quantum-to-classical transition with STS. As a matter of fact, without seeding the OPO, output signal is a squeezed vacuum state, which is then degraded to a STS with a nonzero thermal component by propagation in a lossy channel (state no. 1 in Table I). However, STS obtained in this way are always nonclassical for any value of the loss and the squeezing parameters [37–39].

TABLE I. Characterization, via homodyne tomography, of the $m = 14$ experimental STS in terms of the position and momentum variances, total energy, squeezing factor, and purity. The STS display squeezing in position and antisqueezing in momentum coordinates ($r < 0$).

State no.	$\langle \Delta \hat{x}^2 \rangle$	$\langle \Delta \hat{p}^2 \rangle$	$\langle \hat{a}^\dagger \hat{a} \rangle$	s_{exp}	μ_{exp}
1	0.48 ± 0.03	3.15 ± 0.09	0.41 ± 0.02	0.39 ± 0.01	0.81 ± 0.03
2	0.67 ± 0.04	3.33 ± 0.09	0.50 ± 0.02	0.45 ± 0.01	0.67 ± 0.02
3	0.62 ± 0.04	3.77 ± 0.11	0.60 ± 0.02	0.40 ± 0.02	0.66 ± 0.02
4	0.69 ± 0.05	3.94 ± 0.11	0.66 ± 0.02	0.41 ± 0.02	0.61 ± 0.02
5	0.70 ± 0.05	4.51 ± 0.12	0.80 ± 0.03	0.39 ± 0.02	0.56 ± 0.02
6	0.77 ± 0.05	4.54 ± 0.13	0.83 ± 0.03	0.41 ± 0.02	0.54 ± 0.02
7	0.77 ± 0.05	4.60 ± 0.13	0.84 ± 0.03	0.41 ± 0.02	0.53 ± 0.02
8	0.93 ± 0.06	5.00 ± 0.14	0.98 ± 0.03	0.43 ± 0.02	0.46 ± 0.02
9	0.95 ± 0.06	5.36 ± 0.15	1.08 ± 0.03	0.42 ± 0.01	0.44 ± 0.02
10	0.93 ± 0.07	5.56 ± 0.15	1.12 ± 0.03	0.41 ± 0.02	0.44 ± 0.02
11	1.00 ± 0.07	5.80 ± 0.17	1.20 ± 0.03	0.42 ± 0.02	0.42 ± 0.02
12	1.13 ± 0.07	5.87 ± 0.16	1.25 ± 0.03	0.44 ± 0.02	0.39 ± 0.01
13	1.11 ± 0.08	6.33 ± 0.18	1.36 ± 0.04	0.42 ± 0.02	0.38 ± 0.01
14	1.30 ± 0.08	6.16 ± 0.18	1.36 ± 0.04	0.46 ± 0.02	0.35 ± 0.01

B. Homodyne tomography

We perform state reconstruction of single-mode CV systems by quantum homodyne tomography, i.e., by collecting homodyne data at different LO phases and applying the pattern functions method [1]. This technique allows one to obtain the expectation value of any observable $\hat{O}$ on a given state $\hat{\rho}$ starting from a set of homodyne data $\{(\theta_k,x_k)\}$, x_k being the kth outcome from the measurement of the quadrature (3) at phase θ_k, with $k = 1,\ldots,M$. Upon exploiting the Glauber representation of operators in polar coordinates, the average value of a generic observable $\hat{O}$ may be rewritten as

$$\langle\hat{O}\rangle = \int_0^{\pi}\frac{d\theta}{\pi}\int_{-\infty}^{+\infty} dx\; p(x,\theta)\mathcal{R}[\hat{O}](x,\theta), \tag{10}$$

where $p(x,\theta) = \langle x_\theta|\hat{\rho}|x_\theta\rangle$ is the distribution of quadrature outcomes, with $\{|x_\theta\rangle\}$ the set of eigenvectors of $\hat{x}_\theta$, and $\mathcal{R}[\hat{O}](x,\theta) = \int_{-\infty}^{+\infty} dy|y|\mathrm{Tr}[\hat{O}e^{iy(\hat{x}_\theta - x)}]$ the estimator of the operator ensemble average $\langle\hat{O}\rangle$. For large samples $M \gg 1$, the integral (10) can be recast in the discrete form

$$\langle\hat{O}\rangle \simeq \frac{1}{M}\sum_{k=1}^{M}\mathcal{R}[\hat{O}](x_k,\theta_k). \tag{11}$$

The uncertainty of the estimated value $\langle\hat{O}\rangle$ is ruled by the central limit theorem and scales as $\sqrt{M}$, namely

$$\delta\langle\hat{O}\rangle = \frac{1}{\sqrt{M}}\sqrt{\sum_{k=1}^{M}\frac{[\mathcal{R}[\hat{O}](x_k,\theta_k)]^2 - \langle\hat{O}\rangle^2}{M}}. \tag{12}$$

In order to properly characterize a single-mode prepared in a Gaussian STS, we need to estimate the first two moments of the quadrature operator $\hat{x}_\phi$ and reconstruct the first-moment vector and the CM, as well as the total energy $\hat{a}^\dagger\hat{a}$ of the state. We thus need the following estimators [1]:

$$\mathcal{R}[\hat{x}_\phi](x,\theta) = 2x\,\cos(\theta-\phi), \tag{13a}$$

$$\mathcal{R}[\hat{x}_\phi^2](x,\theta) = (x^2-1)\{1+2\cos[2(\theta-\phi)]\}+1, \tag{13b}$$

$$\mathcal{R}[\hat{a}^\dagger\hat{a}](x,\theta) = \tfrac{1}{2}(x^2-1). \tag{13c}$$

In this way it is possible to compute the average value $\langle\hat{O}\rangle$ and the fluctuations $\langle\Delta\hat{O}^2\rangle \equiv \langle\hat{O}^2\rangle - \langle\hat{O}\rangle^2$ for the observables of interest, together with the corresponding uncertainties (12).

We collect $M = 7000$ homodyne data $\{(x_k,\theta_k)\}$ for each state and address the quantum-to-classical transition by generating $m = 14$ STS with increasing thermal component, as the squeezing is fixed by the geometry of the experimental setup. For all the detected states, we tested the compatibility with the typical form of the STS, i.e., null first-moment vector (4a) and diagonal CM (5). We characterized these states (see Table I) in terms of the position $\langle\Delta\hat{x}^2\rangle$ and momentum $\langle\Delta\hat{p}^2\rangle$ variances; the total energy $N_{\mathrm{tot}} \equiv \langle\hat{a}^\dagger\hat{a}\rangle$. From the measured quadrature variances, the experimental squeezing factor $s_{\mathrm{exp}} = [\langle\Delta\hat{x}^2\rangle/\langle\Delta\hat{p}^2\rangle]^{1/2}$ and purity $\mu_{\mathrm{exp}} = [\langle\Delta\hat{x}^2\rangle\langle\Delta\hat{p}^2\rangle]^{-1/2}$ are obtained. As already mentioned at the beginning of this section, the shot-noise threshold is set at $\langle\Delta\hat{x}^2\rangle = \langle\Delta\hat{p}^2\rangle = 1$, under which the state of the detected single-mode radiation displays genuine quantum squeezing.

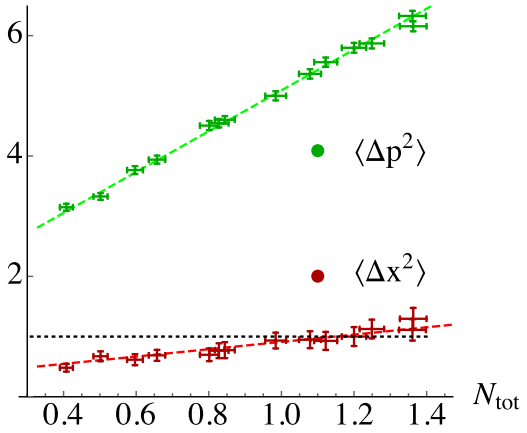

FIG. 2. Tomographic reconstruction of the variances of the squeezed quadrature $\hat{x}$ (red lower dots) and of the antisqueezed quadrature $\hat{p}$ (green upper dots) as a function of the total energy N_{tot}, for $m = 14$ experimental STS. Dashed lines represent linear fits of the experimental data [see Eq. (7)], from which we obtain the number of squeezed photons $n_s \simeq 0.2$. The black dotted horizontal line is the shot-noise level at $\langle\Delta\hat{x}^2\rangle = \langle\Delta\hat{p}^2\rangle = 1$.

The generated STS display squeezing in position quadrature and antisqueezing in momentum quadrature (i.e., we have real and negative squeezing parameter $r < 0$). In Fig. 2 we show the position and momentum variances as a function of the total energy for the $m = 14$ experimentally generated STS. A linear fitting, following Eq. (7), provides the value of the number of squeezed photons $n_s \simeq 0.2$, which corresponds to $\sim$3.7 dB of squeezing. Figure 2 makes apparent the capability of the experimental setup to generate STS on demand by seeding the OPO with a controlled number of thermal photons and, in turn, to monitor the quantum-to-classical transition of a single-mode Gaussian state of light.

C. Fidelity

In order to perform the uncertainties budget, to discuss the statistical distribution of relevant quantities, and to assess the statistical significance of fidelity, we generate $N_{\mathrm{MC}} = 10^3$ Monte Carlo replica data samples (see the Appendix), for each experimental state. Resampled (raw) homodyne data are drawn from Gaussian distributions using the experimental values of Table I to build the average values (4a) and the variances (4b) of the distributions. For all the $m = 14$ STS we apply homodyne tomography and analyze the distribution of the reconstructed states in the neighboring of the experimental target state. Results are shown in Fig. 3 and Fig. 4, using the squeezing-purity plane-$\{s,\mu\}$ representation. Figure 3 focuses on three specific states (number 7, 9, and 13 of Table I) which are closer to the quantum-classical boundary. Target states correspond to black points, whereas the ovoidal regions denote the set of states having fidelity larger than $F > 0.995$ to the target. The darker, stripelike, regions within each balloon correspond to states satisfying the additional constraint of having fluctuations of the total energy (6) at most within one standard deviation.

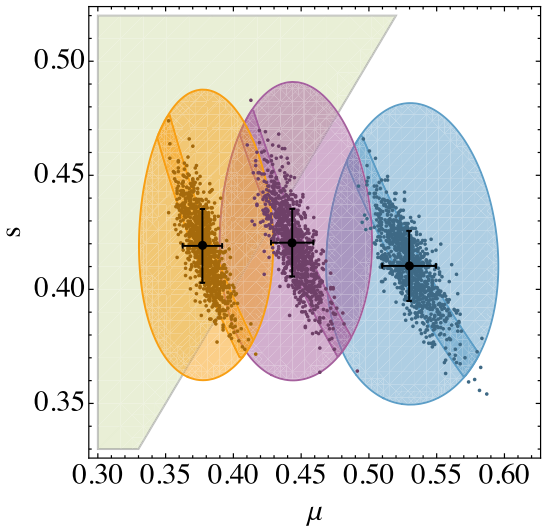

FIG. 3. Statistical distribution of reconstructed STS in the squeezing-purity plane $\{s,\mu\}$. Data come from $N_{\rm MC}$ Monte Carlo resampled set of data for STS (see text and Appendix). From right to left, we have distributions for three experimental STS (state number 7,9 and 13 of Table I), shown as black points with the corresponding bars of precision. The triangularlike region $s > \mu$ contains states with a classical analog. The whole set of reconstructed states are contained in the ovoidal regions, i.e., have fidelity $F > 0.995$ to the corresponding target state. The stripelike regions are obtained adding a constraint to the total energy, i.e., $N_{\rm tot}^{(\rm exp)} - \delta N_{\rm tot}^{(\rm exp)} < \langle \hat{a}^\dagger \hat{a} \rangle < N_{\rm tot}^{(\rm exp)} + \delta N_{\rm tot}^{(\rm exp)}$.

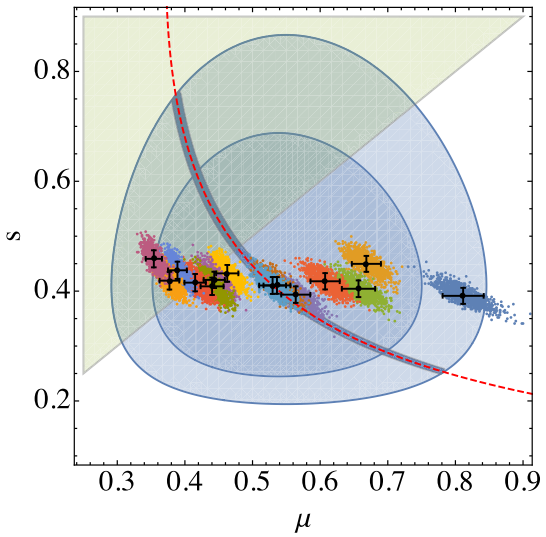

FIG. 4. Statistical distribution of reconstructed STS in the squeezing-purity plane $\{s,\mu\}$ for all the experimental target states in Table I (black points corresponding to states 1 . . . 14 from right to left). The two balloons include states having fidelity to a nonclassical target STS (with $s = 0.41$ and $\mu = 0.53$) larger than $F > 0.90$ (outer balloon) or $F > 0.95$ (inner balloon), respectively, i.e., values commonly recognized as regions of *high fidelity*. The size of the compatibility regions may be reduced by adding energy constraints (as discussed in Fig. 3). As an example, the stripelike region is centered around the red dashed line (state no. 7, $\langle \hat{a}^\dagger \hat{a} \rangle = 0.84$). A significant amount of states may still display opposite classicality properties compared to the target.

As is apparent from the plot, the distribution of STS is concentrated within those stripes. On the other hand, despite the distributions being very sharp in terms of fidelity to their targets (recall that the balloons contains states with fidelity larger than $F \geqslant 0.995$ to the target), their physical properties may be very different. This fact is clearly illustrated looking at nonclassicality, i.e., checking whether the Glauber P function of the state is regular (this happens if $s > \mu$, corresponding to a triangular region in Fig. 3) or singular: states with very high fidelity to a classical or a nonclassical target may not share this property with the target itself.

This effect may be not particularly surprising for target states at the border of the classicality region, even for high values of fidelity. On the other hand, the point becomes far more relevant if values of fidelity commonly used in experiments are considered. In Fig. 4 we show the balloons of states having fidelity $F \geqslant 0.9$ or $F \geqslant 0.95$ to a nonclassical target STS. As is apparent from the plot, *all* the generated STS are contained in the balloons, irrespective of their nonclassicality. The compatibility region may be considerably reduced in size by adding an energy constraint but, nonetheless, a large number of states may still fall in the region of classicality.

Overall, we conclude that fidelity is not a significant figure of merit to assess nonclassicality of STS and should not be employed to benchmark a generation scheme or certify quantum resources for a given protocol.

III. TWO-QUBIT SYSTEMS

In this section we deal with discrete two-qubit systems. In particular, we focus on two-photon polarization states $|HH\rangle$, $|HV\rangle$, $|VH\rangle$, and $|VV\rangle$, and address the reconstruction of statistical mixtures belonging to the class of Werner states:

$$\hat{\rho}^{(w)} = p\,|\Psi^-\rangle\langle\Psi^-| + \frac{1-p}{4}\hat{\mathbb{I}}_4, \tag{14}$$

where $\hat{\mathbb{I}}_4$ is the identity operator in the four-dimensional Hilbert space of two qubits and $|\Psi^-\rangle$ is one of the maximally entangled Bell states

$$|\Phi^\pm\rangle = \frac{|HH\rangle \pm |VV\rangle}{\sqrt{2}} \quad \text{and} \quad |\Psi^\pm\rangle = \frac{|HV\rangle \pm |VH\rangle}{\sqrt{2}}. \tag{15}$$

The parameter $-1/3 \leqslant p \leqslant 1$ tunes the mixture (14) from the maximally mixed state $\hat{\mathbb{I}}_4/4$ for $p = 0$ to the maximally entangled Bell state $|\Psi^-\rangle$ for $p = 1$. In between, the quantum-to-classical transition is located at $p = 1/3$, with entangled states satisfying $p > 1/3$ and separable ones $p < 1/3$.

A. Experimental generation of Werner states

A schematic diagram of experimental setup is sketched in Fig. 5. Photon pairs are generated by type-I down conversion from a couple of beta barium borate (BBO) crystals, in a non-collinear configuration, pumped with a linearly polarized cw 405 nm laser diode, whose effective power on the generating crystals is about 10 mW. The experimental apparatus has been already described in detail in Refs. [40,41]. Here a half-wave

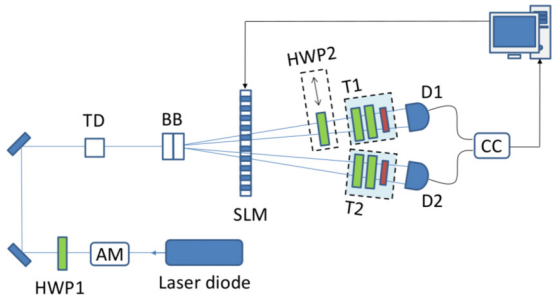

FIG. 5. Schematic diagram of experimental setup. A linearly polarized cw laser diode at 405 nm pumps a couple of BBO crystals cut for type-I down conversion. The horizontal and vertical amplitudes of the photon pairs are balanced by a half-wave plate set along the pump path (HWP1), whereas an additional BBO crystal (TD) is placed on the pump path to compensate the temporal delay. The amplitude modulator (AM) consists of a half-wave plate and polarizer beam splitter. Signal and idler beams travel through the SLM, which provides purification of the generated states. A half-wave plate (HWP2) is inserted on signal path in order to generate the state $\hat{\rho}_\lambda$ (see the text), whereas a quarter-wave plate, a half-wave plate, and a polarizer (sectors T1 and T2) are used for the tomographic reconstruction. Finally, the beams are detected by detectors D1 and D2 and sent to single-photon counting modules (CC).

plate (HWP2 in Fig. 5) has been inserted in front of detector D1 to perform $|\Phi^-\rangle \rightarrow |\Psi^-\rangle$ transformation. A programmable one-dimensional spatial light modulator (SLM), which is a liquid crystal phase mask (64×10 mm) divided in 640 horizontal pixels, each 100 μm wide, is placed on the path of signal and idler beams in order to control the visibility of the generated states. The SLM provides the setup with great flexibility, allowing the experimenter to choose and set the visibility of generated states [42,43]. Eventually, photons are focused in two multimode fibers and sent to single-photon counting modules (CC).

Our experimental apparatus allows us to mix two types of Bell states at a time, either $|\Psi^\pm\rangle$ or $|\Phi^\pm\rangle$. In order to obtain a Werner state (14) we generate the polarization entangled states $\hat{\rho}_\lambda = \lambda|\Psi^-\rangle\langle\Psi^-| + (1-\lambda)|\Psi^+\rangle\langle\Psi^+|$ and the mixed state $\hat{\rho}_{\rm mix} = (|\Phi^+\rangle\langle\Phi^+| + |\Phi^-\rangle\langle\Phi^-|)/2$ [40,44]. Werner states may be obtained by suitably mixing these two states $\hat{\rho}^{(w)} = f_1\hat{\rho}_\lambda + f_2\hat{\rho}_{\rm mix}$ with proper probabilities, given by $f_1 = \frac{1+p}{2}$, $f_2 = \frac{1-p}{2}$, and $\lambda = \frac{2p}{p+1}$. The mixed state $\hat{\rho}_{\rm mix}$ is obtained using the same scheme of Fig. 5 upon removing the HWP2 from the signal path and setting the SLM in order to get $\lambda \simeq 0$. The frequencies f_1 and f_2 are tuned by changing the power of the pump beam with an amplitude modulator (AM). The full range of Werner states may be explored.

The tomographic reconstruction is performed by measuring 16 projective and independent observables in the two-qubit Hilbert space, namely $P_j = |\psi_j\rangle\langle\psi_j|$ (with $j = 1, \ldots, 16$). Different settings of the apparatus, obtained by combining a quarter-wave plate, a half-wave plate, and a polarizer (sectors T1 and T2 in Fig. 5), are employed [45,46]. Each of the 16 measurements correspond to 30 acquisitions, in a time window of 1 s, of coincidence photon counts $\{n_j\}_{j=1}^{16}$, i.e., the outcomes of the projectors P_j.

B. Tomography with MLE

The density matrix of the two-qubit states generated in the experiment has been reconstructed using maximum-likelihood (MLE) tomographic protocol [45,46]. This scheme adopts a suitable parametrization of the density matrix, namely $\hat{\rho}(\mathbb{T}) = T^\dagger T/{\rm Tr}[T^\dagger T]$, where T is a complex lower triangular matrix and $\mathbb{T} = \{t_j\}_{j=1}^{16}$ is the set of 16 parameters characterizing the density matrix. In this way it is ensured that $\hat{\rho}$ is positive and Hermitian (Choleski decomposition). The MLE protocol allows one to recover the set $\mathbb{T}$ by means of a constrained optimization procedure with Lagrange multipliers, which accounts for the normalization condition ${\rm Tr}[\hat{\rho}] = 1$, involving the set of data coming from the 16 experimental measurements. In particular, the logarithmic likelihood functional to be minimized reads

$$\mathcal{L}(\mathbb{T}) = \sum_{j=1}^{16} \frac{[\mathcal{N}\langle\psi_j|\hat{\rho}(\mathbb{T})|\psi_j\rangle - n_j]^2}{2\mathcal{N}\langle\psi_j|\hat{\rho}(\mathbb{T})|\psi_j\rangle}, \tag{16}$$

where $\mathcal{N} = \sum_{j=1}^{4} n_j$ is a constant proportional to the total number of acquisitions.

We experimentally generated $N_{\rm exp} = 4$ two-qubit states not too far from the border between separable and entangled states (see Table II). MLE quantum tomography shows that the reconstructed density matrices do not display the typical X shape of an ideal Werner state (14) with real-valued elements. A possible route to extract the desired Werner state is based on the maximization of the fidelity between the experimental state and the generic Werner state (14). This procedure sounds reasonable and, in principle, may allow one to assess the quantum resources contained in the generated state, as well as to exploit them in order to accomplish quantum tasks. On the other hand, we will show in the following that a fidelity-based inference is in general misleading and should be avoided in assessing the true quantum properties of the experimentally generated state.

C. Fidelity

In order to perform statistical analysis of data and evaluate uncertainties we have resampled photon counts data to obtain $N_{\rm MC} = 10^3$ repeated samples for each of the $N_{\rm exp} = 4$ experimental states (see the Appendix for details). The significance of fidelity may be assessed upon the comparison between two possible strategies to reconstruct quantum properties of the generated states and their distribution. In the first strategy we evaluate properties from the reconstructed states $\hat{\rho}_k^i$ ($k = 1, \ldots, N_{\rm exp}$ and $i = 1, \ldots, N_{\rm MC}$) as obtained by the MLE tomography. In the second strategy we analyze the properties of Werner states $[\hat{\rho}_k^i]^{(w)}$ closest to each reconstructed state $\hat{\rho}_k^i$. We point out that the parameter p characterizing these approximated Werner states maximize $F(\hat{\rho}^i, \hat{\rho}^{(w)})$, where $\hat{\rho}^{(w)}$ is a generic Werner state (14). In Figs. 6(a)–7(a) we can see how the states $[\hat{\rho}_k^i]^{(w)}$ distribute according to p along the horizontal axis.

The first method is based only on tomographic data and provides an average two-qubit state $\overline{\hat{\rho}_k} = \sum_{i=1}^{N_{\rm MC}} \hat{\rho}_k^i/N_{\rm MC}$, which optimizes the likelihood of the experimental data. This average state may be then employed to infer a Werner target state $\hat{\rho}_k^{(w)}$, of the form given in Eq. (14), via a maximization

TABLE II. Statistical analysis of the tomography of $N_{\mathrm{MC}} = 10^3$ two-qubit states, having fidelities $F(\overline{\hat{\rho}_k}, \hat{\rho}_k^{(w)})$ with target Werner of parameter $p_k^{(w)}$. The average values of the least eigenvalue $e_m(\hat{\rho}^{(\tau)})$ and of quantum discord $D(\hat{\rho})$ are reported for both the distributions of tomographic states and of the approximated Werner states.

	State 1	State 2	State 3	State 4
$p_k^{(w)}$	0.32 ± 0.04	0.35 ± 0.04	0.28 ± 0.04	0.44 ± 0.05
$F(\overline{\hat{\rho}_k}, \hat{\rho}_k^{(w)})$	$0.985^{+0.006}_{-0.01}$	$0.988^{+0.005}_{-0.01}$	$0.987^{+0.006}_{-0.01}$	$0.985^{+0.007}_{-0.02}$
$e_m(\overline{\hat{\rho}_k}^{(\tau)})$	0.01 ± 0.03	-0.01 ± 0.03	0.04 ± 0.03	-0.07 ± 0.03
$e_m([\hat{\rho}_k^{(w)}]^{(\tau)})$	0.01 ± 0.03	-0.01 ± 0.03	0.04 ± 0.03	-0.08 ± 0.04
$D(\overline{\hat{\rho}_k})$	0.08 ± 0.02	0.10 ± 0.02	0.06 ± 0.02	0.14 ± 0.02
$D(\hat{\rho}_k^{(w)})$	0.11 ± 0.03	0.14 ± 0.03	0.06 ± 0.02	0.21 ± 0.04

of the fidelity $F(\overline{\hat{\rho}_k}, \hat{\rho}_k^{(w)})$. Upon adopting the second strategy, we obtain a distribution of approximated Werner states, with an average state compatible, at least in principle, with the Werner target state of the first strategy. The parameters $p_k^{(w)}$ characterizing the Werner target states are reported in Table II.

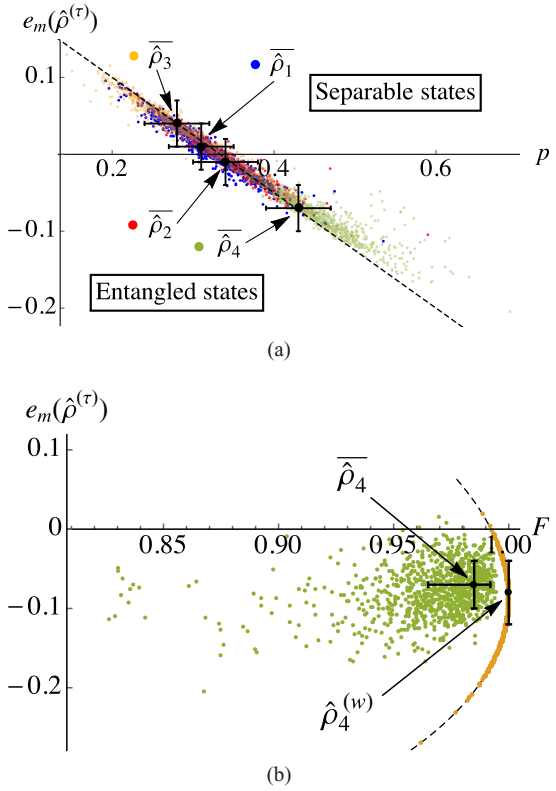

FIG. 6. (a) Distribution of $e_m([\hat{\rho}_k^i]^{(\tau)})$ for 10^3 resampled states as a function of the Werner parameter p. The $N_{\mathrm{exp}} = 4$ average states $\overline{\hat{\rho}_k}$ are highlighted with black dots and error bars, matching the theoretical curve $e_m(\hat{\rho}^{(w)}) = (1 - 3p)/4$ (dashed black line) relative to the negative eigenvalue of the partially transposed ideal Werner state (14). Moreover, it is evident how many states may cross the boundary between entangled and separable states. (b) Distribution of $e_m([\hat{\rho}_4^i]^{(\tau)})$ for 10^3 simulations of the target state $\overline{\hat{\rho}_4}$ as a function of the fidelity $F(\hat{\rho}_4^i, \hat{\rho}_4^{(w)})$ (green dots). The same distribution as a function of $F([\hat{\rho}_4^i]^{(w)}, \hat{\rho}_4^{(w)})$ (orange dots) matches with the theoretical parametric curve (dashed black curve) obtained by evaluating F and e_m of the approximated Werner states. The values of entanglement for the average state $\overline{\hat{\rho}_4}$ and for the target Werner state $\hat{\rho}_4^{(w)}$ are compatible (black dots and error bars).

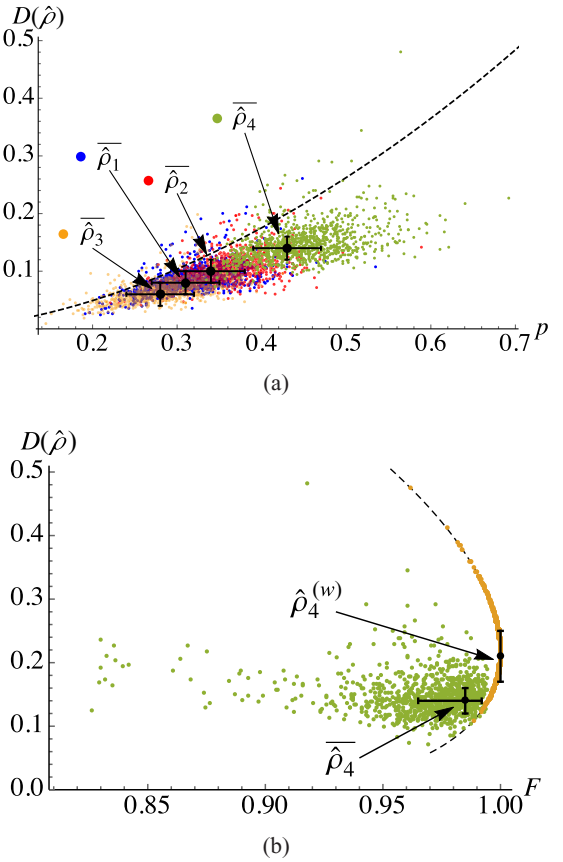

FIG. 7. (a) Distribution of $D(\hat{\rho}_k^i)$ for 10^3 resampled states as a function of the Werner parameter p. The $N_{\mathrm{exp}} = 4$ average states $\overline{\hat{\rho}_k}$ are highlighted with black dots and error bars. The theoretical curve $D(\hat{\rho}^{(w)})$ (dashed black line), relative to the discord of the ideal Werner state (14), is systematically higher than the discord distribution of the tomographic states $\hat{\rho}_k^i$. (b) Distribution of $D(\hat{\rho}_4^i)$ for 10^3 simulations of the target state $\overline{\hat{\rho}_4}$ as a function of the fidelity $F(\hat{\rho}_4^i, \hat{\rho}_4^{(w)})$ (green dots). The same distribution as a function of $F([\hat{\rho}_4^i]^{(w)}, \hat{\rho}_4^{(w)})$ (orange dots) matches with the theoretical parametric curve (dashed black curve) obtained by evaluating F and D of the approximated Werner states. The values of quantum discord for the average state $\overline{\hat{\rho}_4}$ and for the target Werner state $\hat{\rho}_4^{(w)}$ are not compatible (black dots and error bars).

In the following, we analyze how some properties of the quantum states distribute around the target states in terms of fidelity, depending on which of the two strategies has been adopted. In particular, we consider the amount of quantum correlations of two-qubit states, as quantified by entanglement and quantum discord.

1. Entanglement

The separability of two-qubit systems is established by the Peres-Horodecki criterion [47,48]: a quantum state of two qubits $\hat{\rho}$ is separable if and only if the partially transposed density matrix is positive, i.e., $\hat{\rho}^{(\tau)} \geqslant 0$. Thus it is possible to study entanglement or separability properties by evaluating the eigenvalues of the partially transposed density matrix. We compute the minimum of these eigenvalues

$$e_m(\hat{\rho}^{\tau}) \equiv \min\left\{\lambda_n^{\tau}\right\}_{n=1}^{4} \tag{17}$$

for both the considered strategies, i.e., for the distributions of resampled states $\hat{\rho}_k^i$ and of the approximated Werner states $[\hat{\rho}_k^i]^{(w)}$. For a Werner state the minimum eigenvalue, which may assume negative values, is given by $e_m([\hat{\rho}^{(w)}]^{\tau}) = (1 - 3p)/4$.

In Fig. 6(a) we plot the distribution of $e_m(\hat{\rho}^{\tau})$ as a function of the Werner parameter p for all the $N_{\mathrm{MC}} = 10^3$ resampled states, with average tomographic states $\overline{\hat{\rho}_k}$. We note that the average states arrange along the curve of the theoretical behavior for a Werner state and that the resampled states follow the same prediction (see Table II). Nonetheless, there is evidence of some states generated from a separable experimental state in the entangled region, and vice versa. This first observation reveals that statistical fluctuations in an experiment may still produce quantum states with properties radically different from the expected ones, such as separability and entanglement.

In Fig. 6(b), we focus on the most entangled state $\overline{\hat{\rho}_4}$ and compare the distribution of the resampled states and of the corresponding Werner states, in terms of $e_m(\hat{\rho}^{\tau})$ and fidelity with the target state $\hat{\rho}_4^{(w)}$. In this way we can highlight the differences between the two possible strategies for data analysis, i.e., between the evaluation of the properties of the direct tomographic states and the approximated Werner states. This second strategy compels the resampled states to follow the single-parameter Werner state (14) and, thus, to force the distribution of the least eigenvalue $e_m([\hat{\rho}_k^{(w)}]^{(\tau)})$ according to the theoretical prediction (dashed black curve in the plot). In this way, we obtain a distribution of Werner states having, obviously, very high values of fidelity with the target (Werner) state. On the other hand, tomographic states display lower values of fidelity with the target state, but $e_m(\hat{\rho}^{\tau})$ is evaluated directly from the tomographic density matrices. From the statistical analysis, we conclude that the estimated value of $e_m(\hat{\rho}^{\tau})$ is compatible within errors for both the adopted strategies. We will see in the following that these two strategies may lead to different and noncompatible results for another property of quantum states, the quantum discord.

2. Quantum discord

Another widely adopted measure of the amount of quantum correlations in a state $\hat{\rho}$ is the quantum discord [49,50], which is defined starting from two equivalent definitions, in the classical domain, of the mutual information, i.e., the total amount of correlations of $\hat{\rho}$:

$$\mathcal{I}(\hat{\rho}) = S(\hat{\rho}_A) + S(\hat{\rho}_B) - S(\hat{\rho}), \tag{18a}$$

$$\mathcal{J}_A(\hat{\rho}) = S(\hat{\rho}_B) - \min \sum_j c_j S(\hat{\rho}_{B|j}), \tag{18b}$$

where $\hat{\rho}_A$ ($\hat{\rho}_B$) is the reduced density matrix of $\hat{\rho}$ for the subsystems A (or B) and $S(\hat{\rho}) = -\mathrm{Tr}[\hat{\rho}\log_2(\hat{\rho})]$ is the von Neumann entropy. While the first definition (18a) is based only on the von Neumann entropy, the second one in Eq. (18b) accounts for all the classical correlations that can be detected by local projective measurements only on a subsystem. Here $\hat{\rho}_{B|j} = \mathrm{Tr}_A[\hat{\Pi}_j\hat{\rho}\,\hat{\Pi}_j]/\pi_j$ is the reduced state of B conditioned to the set of projectors $\{\hat{\Pi}_j\}$, with probability $\pi_j = \mathrm{Tr}[\hat{\Pi}_j\hat{\rho}\,\hat{\Pi}_j]$ for the outcome j, and the minimum in Eq. (18b) is taken over all the possible $\{\hat{\Pi}_j\}$. A similar definition applies for local measurements on subsystem B. The quantum discord is then evaluated as the residual information stemming from the difference of the two definitions in Eq. (18), which has a pure quantum character:

$$D(\hat{\rho}) \equiv \mathcal{I}(\hat{\rho}) - \mathcal{J}_A(\hat{\rho}). \tag{19}$$

For a Werner state (14) the quantum discord can be analytically evaluated:

$$D(\hat{\rho}^{(w)}) = \frac{1+3p}{4}\log_2(1+3p) + \frac{1-p}{4}\log_2(1-p) - \frac{1+p}{2}\log_2(1+p). \tag{20}$$

In Fig. 7(a) we plot the quantum discord $D(\hat{\rho}_k^i)$ for all the $N_{\mathrm{MC}} = 10^3$ resampled states, with average tomographic states $\overline{\hat{\rho}_k}$, as a function of the Werner parameter p. The theoretical behavior of Eq. (20), represented in the figure by a dashed curve, puts in evidence the high discrepancy with the quantum discord computed for the tomographic states. The approximation to Werner states leads to a systematic overestimation of the quantum discord for the two-qubit states (see also Table II). We can enforce this result by looking at the distribution of the quantum discord relative to the single set of states $\hat{\rho}_4^i$ only, as a function of the fidelity with the corresponding target Werner state $\hat{\rho}_4^{(w)}$ [see Fig. 7(b)]. Most of the states are contained in a region of high values of fidelity, thus suggesting that the approximation to an average Werner state could be correct. Nonetheless, if we consider the distribution of the approximated Werner states, we observe that the values of fidelity increase, but the value of quantum discord of the target Werner state $\hat{\rho}_4^{(w)}$ is out of the limits of compatibility with the average quantum discord $D(\overline{\hat{\rho}_4})$. This suggests that the second strategy employing the approximation to Werner states reveals to be too drastic, as it does not account properly for the actual tomographic reconstruction of the density matrix.

We can conclude that, even though high values of fidelity between a target state and a tomographic state are achieved, the properties of the two can be very different. On an extreme level, we can look at the distribution of the fidelity between the most classical states we generated, $\hat{\rho}_3^i$, and, at the opposite, the most

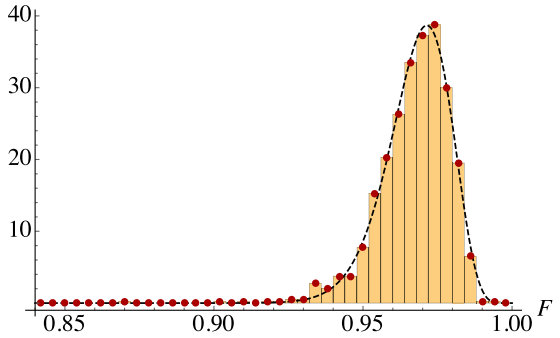

FIG. 8. Histogram shows the distribution of $F(\hat{\rho}_3^i, \hat{\rho}_4^{(w)})$, i.e., the fidelity between a set of separable states and an entangled target state. The data are well fitted by a β distribution, centered around $F \approx 0.97$.

entangled one as the target state, namely $\hat{\rho}_4^{(w)}$. The probability density histogram in Fig. 8 shows that the two kinds of states should result compatible with a level of fidelity $F \approx 0.97$, even though they possess clearly different properties.

IV. CONCLUSIONS

In conclusion, we have addressed quantum state reconstruction for DV and CV quantum optical systems and experimentally analyzed the significance of fidelity as a figure of merit to assess the properties of the reconstructed state. State reconstruction, in the two cases, has been performed adopting homodyne and MLE tomography techniques. One of the most natural ways to link the tomographic results to the target states, i.e., the quantum states supposed to be generated by the designed experimental setup, is the evaluation of fidelity. In order to study the relation between fidelity and the experimental states, we performed statistical analysis using Monte Carlo sampling of each experiment, regenerating sets of $N_{\rm MC} = 10^3$ data samples, and analyzing the distribution of some of their main properties as a function of fidelity.

In the CV framework, we employed a thermal-state seeded OPO cavity, an experimental configuration which allows one to generate STS on demand. The accurate control of the thermal and squeezing component of the apparatus allows us to address the quantum-to-classical transition for these states. Our results show that even for high values of fidelity and imposing energy constraints, one may find neighboring states in terms of fidelity which, however, not share the same quantum or classical properties.

In the DV context, we experimentally obtained pairs of polarized photons from type-I down conversion and conveniently generate the Werner mixed states. This one-parameter family of states allowed us to analyze the nonclassical properties of two-qubit states in terms of entanglement or separability and to evaluate the amount of quantum correlations by means of the quantum discord. We found that a fidelity based approximation of the tomographic states by Werner states may lead to an overestimation, e.g., of the quantum discord. Moreover, high values of fidelity may occur between two very different states in terms of their separability properties.

Overall, we conclude that while fidelity is a good measure of geometrical proximity in the Hilbert space it should not be used as the sole benchmark to certify quantum properties [20–25], which should be rather estimated tomographically in a direct way, or using a suitable witness operator [1,4].

ACKNOWLEDGMENTS

This work has been supported by UniMI through the UNIMI14 Grant No. 15-6-3008000-609 and the H2020 Transition Grant No. 15-6-3008000-625, and by EU through the H2020 Project QuProCS (Grant Agreement No. 641277).

APPENDIX: EVALUATION OF UNCERTAINTIES BY MONTE CARLO RESAMPLING

In order to avoid the limitations of finite samples and the influence of systematic unpredictable errors that could be present in an experiment, we evaluate uncertainties by Monte Carlo resampling of data, according to standard metrological prescriptions [51] valid for any statistical models having a single output quantity and input quantities with arbitrary distribution. Here we provide a brief summary of the main assumptions and principles.

The measured quantities of interest X_i are random variables distributed according to a given probability density function (PDF) $\mathcal{G}(X_i)$. In particular, we assume normal distributions characterized by mean value $\langle x_i \rangle$ and standard deviation δx_i. Monte Carlo evaluation of uncertainties is based on sampling random outcomes from $\mathcal{G}(X_i)$ according to experimental data, which themselves fix the average values and the standard deviations. In particular, as described in the main text, the considered experimental measurements, for CV systems, correspond to homodyne detection of the radiation field quadratures, whereas for DV systems we perform coincidence photon counting measurements of polarized photons. Starting from experimental results, we generate $N_{\rm MC} = 10^3$ resampled replicas of the experiments, thus building a significative sample for the statistical analysis.

[1] G. M. D'Ariano, M. G. A. Paris, and M. F. Sacchi, Adv. Imag. Electr. Phys. **128**, 205 (2003).
[2] M. G. A. Paris and J. Řeháček, *Quantum State Estimation*, Lecture Notes in Physics Vol. 649 (Springer, New York, 2004).
[3] A. I. Lvovsky and M. G. Raymer, Rev. Mod. Phys. **81**, 299 (2009).
[4] C. Schwemmer, L. Knips, D. Richart, H. Weinfurter, T. Moroder, M. Kleinmann, and O. Gühne, Phys. Rev. Lett. **114**, 080403 (2015).
[5] M. Beck, D. T. Smithey, and M. G. Raymer, Phys. Rev. A **48**, R890 (1993).
[6] A. Ourjoumtsev, R. Tualle-Brouri, and P. Grangier, Phys. Rev. Lett. **96**, 213601 (2006).
[7] A. Ourjoumtsev, H. Jeong, R. Tualle-Brouri, and P. Grangier, Nature (London) **448**, 784 (2007).
[8] E. T. Jaynes, Phys. Rev. **106**, 620 (1957); **108**, 171 (1957).
[9] V. Bužek, R. Derka, G. Adam, and P. L. Knight, Ann. Phys. (N.Y.) **266**, 454 (1998).

[10] S. Olivares and M. G. A. Paris, Phys. Rev. A **76**, 042120 (2007).
[11] G. Zambra, A. Andreoni, M. Bondani, M. Gramegna, M. Genovese, G. Brida, A. Rossi, and M. G. A. Paris, Phys. Rev. Lett. **95**, 063602 (2005).
[12] K. Banaszek and I. A. Walmsley, Opt. Lett. **28**, 52 (2003).
[13] J. Řeháček, Z. Hradil, O. Haderka, J. Peřina, Jr., and M. Hamar, Phys. Rev. A **67**, 061801(R) (2003).
[14] A. Uhlmann, Rep. Math. Phys. **9**, 273 (1976).
[15] C. A. Fuchs and J. van de Graaf, IEEE Trans. Inf. Theory **45**, 1216 (1999).
[16] C. F. Roos, G. P. T. Lancaster, M. Riebe, H. Häffner, W. Hänsel, S. Gulde, C. Becher, J. Eschner, F. Schmidt-Kaler, and R. Blatt, Phys. Rev. Lett. **92**, 220402 (2004).
[17] J. Fulconis, O. Alibart, J. L. O'Brien, W. J. Wadsworth, and J. G. Rarity, Phys. Rev. Lett. **99**, 120501 (2007).
[18] D. Riste, M. Dukalski, C. A. Watson, G. de Lange, M. J. Tiggelman, Ya. M. Blanter, K. W. Lehnert, R. N. Schouten, and L. DiCarlo, Nature (London) **502**, 350 (2013).
[19] L. Steffen, Y. Salathe, M. Oppliger, P. Kurpiers, M. Baur, C. Lang, C. Eichler, G. Puebla-Hellmann, A. Fedorov, and A. Wallraff, Nature (London) **500**, 319 (2013).
[20] C. Kurz, M. Schug, P. Eich, J. Huwer, P. Müller, and J. Eschner, Nat. Commun. **5**, 5527 (2014).
[21] F. Dolde, V. Bergholm, Y. Wang, I. Jakobi, B. Naydenov, S. Pezzagna, J. Meijer, F. Jelezko, P. Neumann, T. Schulte-Herbrüggen, J. Biamonte, and J. Wrachtrup, Nat. Commun. **5**, 3371 (2014).
[22] K. De Greve, P. L. McMahon, L. Yu, J. S. Pelc, C. Jones, C. M. Natarajan, N. Young Kim, E. Abe, S. Maier, C. Schneider *et al.*, Nat. Commun. **4**, 2228 (2013).
[23] J. J. Pla, K. Y. Tan, J. P. Dehollain, W. H. Lim, J. J. L. Morton, F. A. Zwanenburg, D. N. Jamieson, A. S. Dzurak, and A. Morello, Nature (London) **496**, 334 (2013).
[24] J. Goldwin, M. Trupke, J. Kenner, A. Ratnapala, and E. A. Hinds, Nat. Commun. **2**, 418 (2011).
[25] D. Leibfried, B. DeMarco, V. Meyer, D. Lucas, M. Barrett, J. Britton, W. M. Itano, B. Jelenković, C. Langer, T. Rosenband, and D. J. Wineland, Nature (London) **422**, 412 (2003).
[26] M. Ban, Phys. Rev. A **69**, 054304 (2004).
[27] C. M. Caves and K. Wodkiewicz, Phys. Rev. Lett. **93**, 040506 (2004).
[28] V. Dodonov, J. Phys. A **45**, 032002 (2012).
[29] M. Bina, A. Mandarino, S. Olivares, and M. G. A. Paris, Phys. Rev. A **89**, 012305 (2014).
[30] A. Mandarino, M. Bina, S. Olivares, and M. G. A. Paris, Int. J. Quant. Inf. **12**, 1461015 (2014).
[31] C. Benedetti, A. P. Shurupov, M. G. A. Paris, G. Brida, and M. Genovese, Phys. Rev. A **87**, 052136 (2013).
[32] I. Bengtsson and K. Zyczkowski, *Geometry of Quantum States* (Cambridge University Press, Cambridge, UK, 2006).
[33] P. Marian and T. A. Marian, Phys. Rev. A **86**, 022340 (2012).
[34] R. W. P. Drever, J. L. Hall, F. V. Kowalski, J. Hough, G. M. Ford, A. J. Munley, and H. Ward, Appl. Phys. B **31**, 97 (1983).
[35] S. Cialdi, C. Porto, D. Cipriani, S. Olivares, and M. G. A. Paris, Phys. Rev. A **93**, 043805 (2016).
[36] H. A. Bachor and T. C. Ralph, *A Guide to Experiments in Quantum Optics* (Wiley-VCH, Weinheim, 2004).
[37] A. R. Rossi, S. Olivares, and M. G. A. Paris, J. Mod. Opt. **51**, 1057 (2004).
[38] A. Ferraro, S. Olivares, and M. G. A. Paris, *Gaussian States in Quantum Information* (Bibliopolis, Napoli, 2005).
[39] S. Olivares, Eur. Phys. J. Special Topics **203**, 3 (2012).
[40] S. Cialdi, F. Castelli, I. Boscolo, and M. G. A. Paris, Appl. Opt. **47**, 1832 (2008).
[41] S. Cialdi, F. Castelli, and M. G. A. Paris, J. Mod. Opt. **56**, 215 (2009).
[42] S. Cialdi, D. Brivio, and M. G. A. Paris, Appl. Phys. Lett. **97**, 041108 (2010).
[43] S. Cialdi, D. Brivio, A. Tabacchini, A. M. Kadhim, and M. G. A. Paris, Opt. Lett. **37**, 3951 (2012).
[44] S. Cialdi, D. Brivio, E. Tesio, and M. G. A. Paris, Phys. Rev. A **84**, 043817 (2011).
[45] K. Banaszek, G. M. D'Ariano, M. G. A. Paris, and M. F. Sacchi, Phys. Rev. A **61**, 010304(R) (1999).
[46] D. F. V. James, P. G. Kwiat, W. J. Munro, and A. G. White, Phys. Rev. A **64**, 052312 (2001).
[47] A. Peres, Phys. Rev. Lett. **77**, 1413 (1996).
[48] M. Horodecki, P. Horodecki, and R. Horodecki, Phys. Lett. A **223**, 1 (1996).
[49] H. Ollivier and W. H. Zurek, Phys. Rev. Lett. **88**, 017901 (2001).
[50] L. Henderson and V. Vedral, J. Phys. A **34**, 6899 (2001).
[51] BIPM, IEC, IFCC, ILAC, ISO, IUPAC, IUPAP, and OIML, *Evaluation of Measurement Data–Supplement 1 to the Guide to the Expression of Uncertainty in Measurement–Propagation of Distributions Using a Monte Carlo Method* (JCGM 101, 2008), http://www.bipm.org/utils/common/documents/jcgm/JCGM_101_2008_E.pdf.